# Journal of Materials Chemistry B



## **PAPER**

View Article Online
View Journal | View Issue



Cite this: *J. Mater. Chem. B*, 2025, **13**, 10584

# SN-38-cholesterol NPs-loaded PDA NPs/agarose & pluronic F-127 hydrogel system for controlled chemo-phototherapy in tumor-localized treatment†

Zhixiang Liu, Da Yoshitaka Koseki, Db Mengheng Yang, Da Keita Tanita and Hitoshi Kasai\*

Pluronic F-127 (PF-127) has low mechanical strength at low concentrations and a high gel-sol transition temperature at high concentrations, which limits its use as a controlled drug-release carrier. To address this issue while preserving the hydrogel's high biocompatibility, we developed a hydrogel system consisting of polydopamine nanoparticles (PDA NPs), agarose, and PF-127 (PDA/APF) in which agarose forms a secondary network and PDA NPs enhance hydrogen bonding in the network, thereby improving the mechanical strength and stability of the hydrogel. This modification prolonged the hydrogel's degradation period to approximately seven days and maintained gel-sol transition temperature at 59.0 °C. We incorporated SN-38-cholesterol NPs into the hydrogel system for sustained chemotherapy. Upon 808 nm near infrared (NIR) irradiation, the hydrogel system behaved as expected by releasing SN-38-cholesterol NPs through subsequent hydrogel degradation induced by the embedded PDA NPs. *In vivo* studies showed that the hydrogel system effectively inhibited tumor growth in mice following photothermal therapy with NIR light. The use of the PDA/APF hydrogel system is a promising strategy for controlled localized cancer therapy, combining chemotherapy and photothermal therapy for enhanced efficacy.

Received 28th April 2025, Accepted 8th July 2025

DOI: 10.1039/d5tb00994d

rsc.li/materials-b

#### 1. Introduction

Cancer is a major public health concern worldwide, <sup>1,2</sup> with chemotherapy as the primary treatment choice. <sup>3,4</sup> However, monotherapy for malignant tumors often leads to drug resistance, resulting in reduced efficacy or treatment failure. <sup>4,5</sup> To overcome this challenge, a combination of different therapeutic strategies to enhance the effectiveness of chemotherapy has become the dominant approach in clinical oncology. <sup>5</sup> These strategies include radiotherapy, <sup>6</sup> immunotherapy, <sup>7</sup> photodynamic therapy, <sup>8</sup> and photothermal therapy (PTT). <sup>9,10</sup> Recently, PTT has emerged as a novel strategy for cancer treatment because of its ability to induce tumor cell ablation through hyperthermia while simultaneously reducing interstitial fluid pressure and improving blood circulation. <sup>11</sup> Furthermore, when combined with

Recently, nanotechnology, in particular, nanocarriers and drug nanocrystals (NCs), has gained significant attention for cancer treatment. Due to the high permeability of tumor vasculature, nanoparticles (NPs) can passively accumulate at tumor sites through the enhanced permeability and retention effect.<sup>13</sup> Additionally, the functionalizing nanoparticles with antibodies or ligands can further enhance their tumortargeting capabilities. 14 Meanwhile, Drug NCs are nanometersized drug particles stabilized using appropriate stabilizers. 15,16 Compared to conventional small-molecule drugs, drug NCs offer the advantages of superior tumor targeting, enhanced retention, and the ability to penetrate deep into solid tumors, leading to increased anticancer efficacy. 17 Furthermore, compared with other nanocarrier-based drug delivery systems, drug NCs demonstrate a higher drug-loading capacity and improved biocompatibility. 18,19 We have previously developed novel drug NCs using a carrier- and stabilizer-free reprecipitation method. 20-23 For example, SN-38-cholesterol (SN-38-chol)24 and camptothecin-trimethyl lock25 NCs require no stabilizers and minimal organic solvents, resulting in lower toxicity, high drug-loading capacity, and excellent stability.

chemotherapy, PTT enhances the sensitivity of tumor cells to conventional drugs. 11,12

<sup>&</sup>lt;sup>a</sup> Institute of Multidisciplinary Research for Advanced Materials, Tohoku University, 2-1-1 Katahira, Aoba, Sendai, Miyagi 980-8577, Japan. E-mail: kasai@tohoku.ac.jp

b Department of Life and Environmental Sciences, Faculty of Bioresource Sciences, Prefectural University of Hiroshima, 5562 Nanatsuka, Shobara, Hiroshima 727-0023, Japan

 $<sup>\</sup>dagger$  Electronic supplementary information (ESI) available. See DOI: https://doi.org/10.1039/d5tb00994d

Additionally, near-infrared (NIR)-responsive NPs, including gold, <sup>26</sup> titanium oxide, <sup>27</sup> and polydopamine nanoparticles (PDA NPs), <sup>28</sup> can serve as photothermal agents for PTT. NIR light in the first window (650–900 nm) exhibits enhanced tissue penetration and minimal absorption by healthy tissues, making it particularly advantageous for *in vivo* tumor treatment. <sup>29,30</sup>

Although NPs exhibit certain tumor-targeting capabilities, their accumulation at tumor sites remains relatively low. Consequently, localized drug delivery strategies for enhancing drug retention at tumor sites have gained increasing attention.<sup>31</sup> Hydrogels are effective local drug delivery systems that can encapsulate therapeutic agents and achieve controlled release in response to external stimuli.<sup>32</sup> Thermosensitive hydrogels are a unique class of hydrogels whose physicochemical properties change with temperature.<sup>33</sup> Well-known thermosensitive hydrogel materials include poly(*N*-isopropylacrylamide) (pNIPAM),<sup>34</sup> polyacrylic acid,<sup>33</sup> chitosan,<sup>35</sup> and poly(ethylene oxide)-poly(propylene oxide)-poly(ethylene oxide) (PEO-PPO-PEO, Pluronics).<sup>36</sup> Among these materials, the Pluronic F-127 (PF-127) hydrogel is widely recognized for its unique sol-gel-sol transition properties. At low temperatures, PF-127 exhibits high solubility owing to the formation of hydrogen bonds. As the temperature increases, the hydrogen bonds between the water molecules and the hydrophilic chain termini break, leading to enhanced interactions between the hydrophobic poly(propylene oxide) chains<sup>37</sup> This results in the formation of a cubic crystalline structure, thereby transitioning the solution to a gel state.<sup>38</sup> Upon further temperature elevation, the heat-induced disruption of the micellar crystalline structure causes the hydrogel to revert to the sol state.<sup>39</sup> Owing to its distinct thermosensitive properties, PF-127 is frequently employed as an injectable in situ gel formulation for sustained drug release. 40,41 However, its low mechanical strength and rapid dissolution in biological fluids pose challenges for its application as a sustained drug-release carrier. Meanwhile, PF127 hydrogel requires a high concentration to achieve adequate stability; however, at such concentrations, the gel-sol transition temperature often exceeds 80 °C, which significantly limits its practical applicability.42

Numerous strategies have been explored to enhance the mechanical strength of PF-127 hydrogels, including chemical modifications of the PF-127 backbone, incorporation of other hydrophilic polymers to form a dual-network structure, enhancement of intermolecular hydrogen bonding, and the addition of chemical cross-linkers. 43-45 To mitigate the potential side effects associated with crosslinkers and chemical modifications, we introduced agarose as a highly biocompatible secondary network component to reinforce the mechanical strength of PF-127 hydrogels. 46 Additionally, agarose contains abundant hydroxyl functional groups that facilitate hydrogen bonding within the hydrogel system, thereby improving its physical stability. Furthermore, we selected PDA NPs, known for their excellent photothermal conversion efficiency and biocompatibility, as NIR-responsive photothermal agents. 47 The amine groups of PDA NPs are expected to form hydrogen bonds with the hydroxyl group in PF-127 and agarose, thereby enhancing the mechanic strength of the hydrogel system.

In this study, we developed an *in situ* drug-loaded hydrogel system based on a composite PF-127 and agarose hydrogel loaded with PDA NPs, which we designated as PDA/APF hydrogel (Fig. 1). The hydrogel system was used to encapsulate SN-38-chol NPs for sustained drug release, facilitating combined chemotherapy and PTT to enhance antitumor efficacy. This newly developed PDA/APF hydrogel system represents a significant advancement in controlled drug release for chemophotothermal cancer therapy.

## 2. Results

#### 2.1. Preparation of SN-38-chol NPs and PDA NPs

SN-38-chol NPs were prepared using a reprecipitation method. SN-38-chol is a prodrug derivative of SN-38 in which cholesterol is conjugated to SN-38 to enhance its lipophilicity. During reprecipitation, SN-38-chol dissolved in tetrahydrofuran (THF) was rapidly injected into deionized water, resulting in the rapid formation of drug NCs (Fig. 2a).

The scanning electron microscopy (SEM) image of the SN-38-chol NPs (Fig. 2b) reveals generally spherical particles with an average diameter of approximately 71 nm. This is smaller than the size measured by dynamic light scattering (DLS, 119.1 nm; Fig. 2d), as expected, since DLS reflects the hydrodynamic diameter of nanoparticles in solution, whereas SEM captures their physical size in the dry state. Additionally, according to the DLS results (Fig. 2e), although the polydispersity index of the SN-38-chol NPs slightly increased over 21 d, the particle size remained unchanged, demonstrating excellent stability. Fig. 2c shows an SEM image of the PDA NPs, which appeared smaller than the DLS-measured size (143.2 nm, Fig. 2d), with an observed diameter of approximately 116 nm. The size of the PDA NPs could be easily tuned by adjusting the synthesis time and pH, as detailed in Table S1 (ESI†). PDA NPs exhibit good stability (Fig. S1, ESI†); however, prolonged storage in water can lead to NPs sedimentation, which requires resuspension by shaking before use. In this study, larger PDA NPs ( $\sim 400$  nm) were selected due to their lower clearance rate, making them more suitable for the intended application.

#### 2.2. Design and preparation of PDA/APF composite hydrogel

Considering that this study employs high temperature photothermal ablation to eliminate tumor cells, the optimal therapeutic temperature range for *in vivo* PTT is considered to be between 48 °C and 65 °C, where effective tumor ablation can be achieved without causing excessive damage to surrounding healthy tissues. <sup>48</sup> Temperatures below this range fail to achieve tumor ablation, whereas temperatures exceeding this range risk damaging healthy tissues. <sup>49,50</sup> As illustrated in Fig. S2 (ESI†), we investigated the NIR-triggered temperature response of the PF hydrogels with varying PDA NPs concentrations over a 5-min irradiation period. Increasing the content of PDA NPs intensified the temperature increase in the hydrogel system. Specifically, 0.6 mg g<sup>-1</sup> (weight of PDA NPs/weight of hydrogel) PDA NPs maintained the hydrogel within the ideal PTT temperature

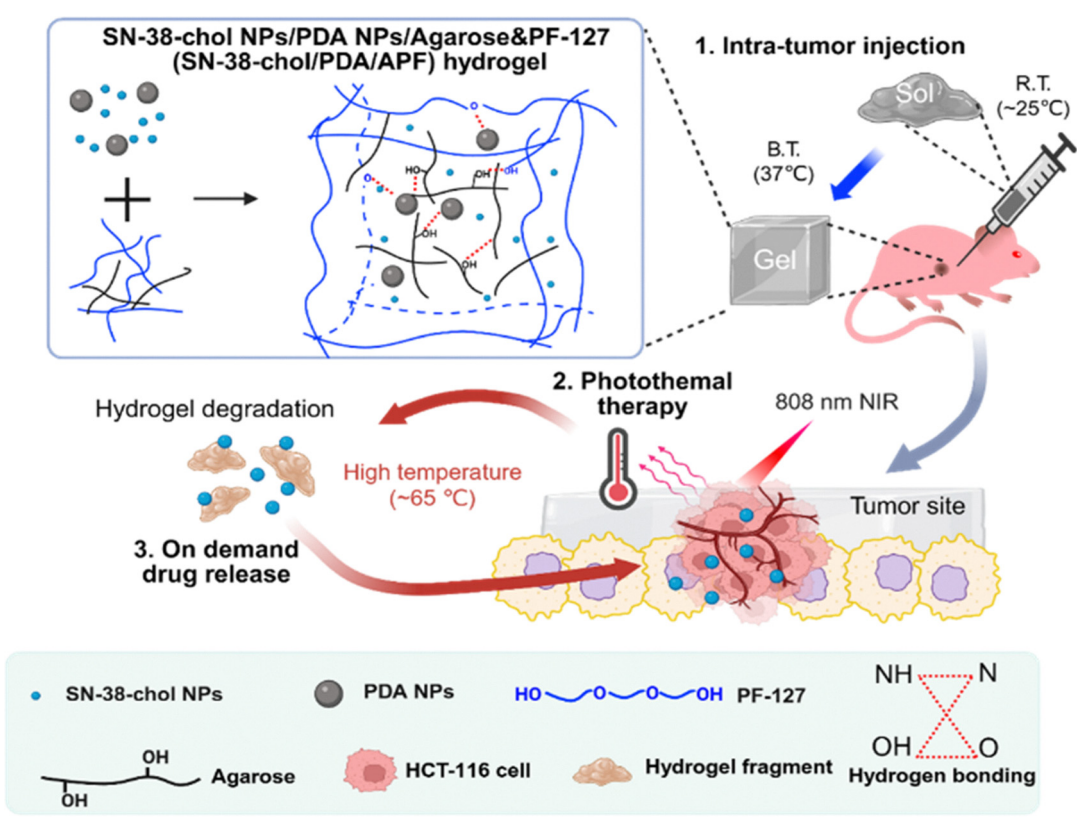


Fig. 1 Schematic diagram of the SN-38-cholesterol and polydopamine nanoparticle/agarose & PF-127 (SN-38-chol/PDA/APF) hydrogel and the combined chemotherapy and photothermal treatment regimen.

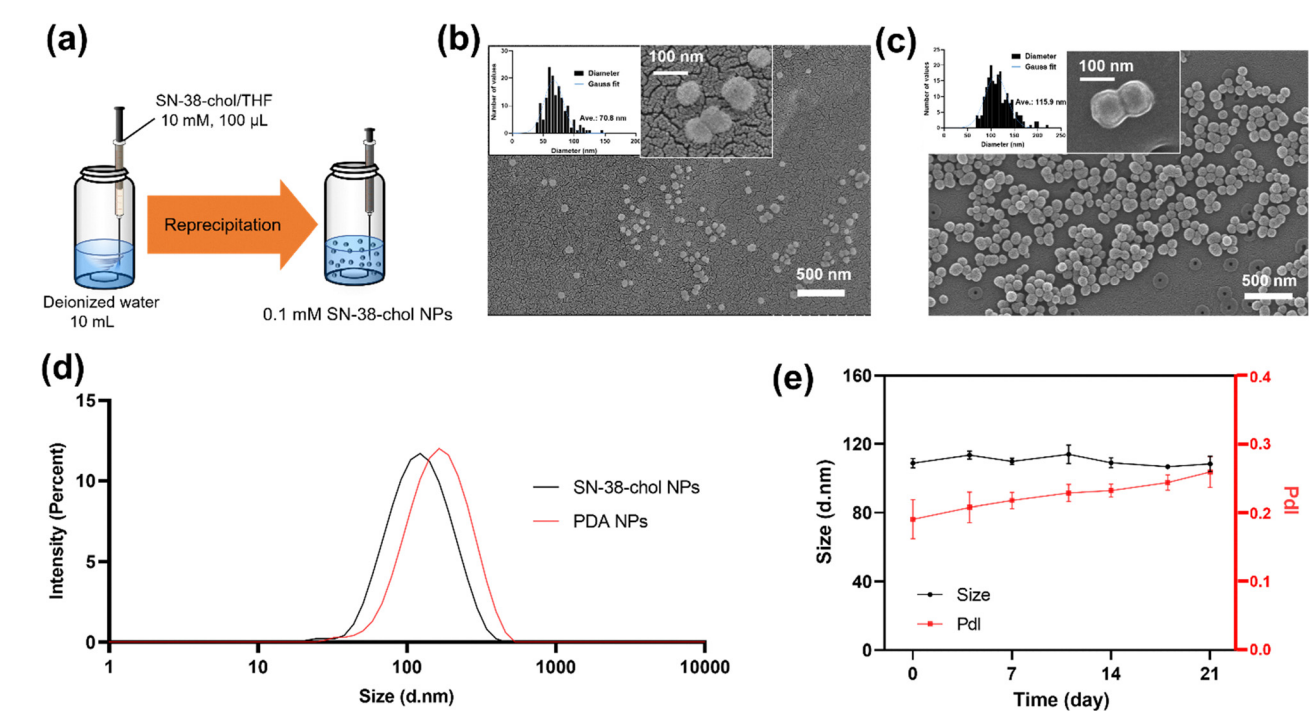


Fig. 2 Characterization of nanoparticles. (a) Schematic diagram of reprecipitation method. (b) Scanning electron microscopy (SEM) image of SN-38-chol NPs. (c) SEM image of PDA NPs. (d) Dynamic light scattering of SN-38-chol NPs and PDA NPs. (e) The changes in particle size and polydispersity index of SN-38-chol NPs over 21 days.

range, whereas  $0.9 \text{ mg g}^{-1}$  led to excessively high temperatures. After 5 min of NIR irradiation, the temperature of the 0.6 mg  $g^{-1}$ PDA/APF composite hydrogel stabilized between 60 °C and 65 °C, with a peak temperature of 63.5 °C. Consequently, 0.6 mg g<sup>-1</sup> PDA was chosen as the baseline for subsequent experiments. To ensure that the NIR-induced temperature increase triggers the gel-sol transition of the PF-127 hydrogel, the gel-sol transition point must be maintained below 60 °C. As shown in Fig. 3a, the gel-sol transition point of the hydrogel increased rapidly at higher PF-127

concentrations, whereas the sol-gel transition point decreased correspondingly. The critical gelation concentration of PF-127 was determined to be 15 wt%. Additionally, the degradation rate of the hydrogel was influenced by the PF-127 concentration. Lower concentrations resulted in rapid degradation, with complete disintegration occurring within approximately 12 h. As the PF-127 concentration increased, the degradation period was prolonged, reaching approximately 5 d at 30 wt% (Fig. 3b). Low PF-127 concentrations cause the PF hydrogel system to degrade

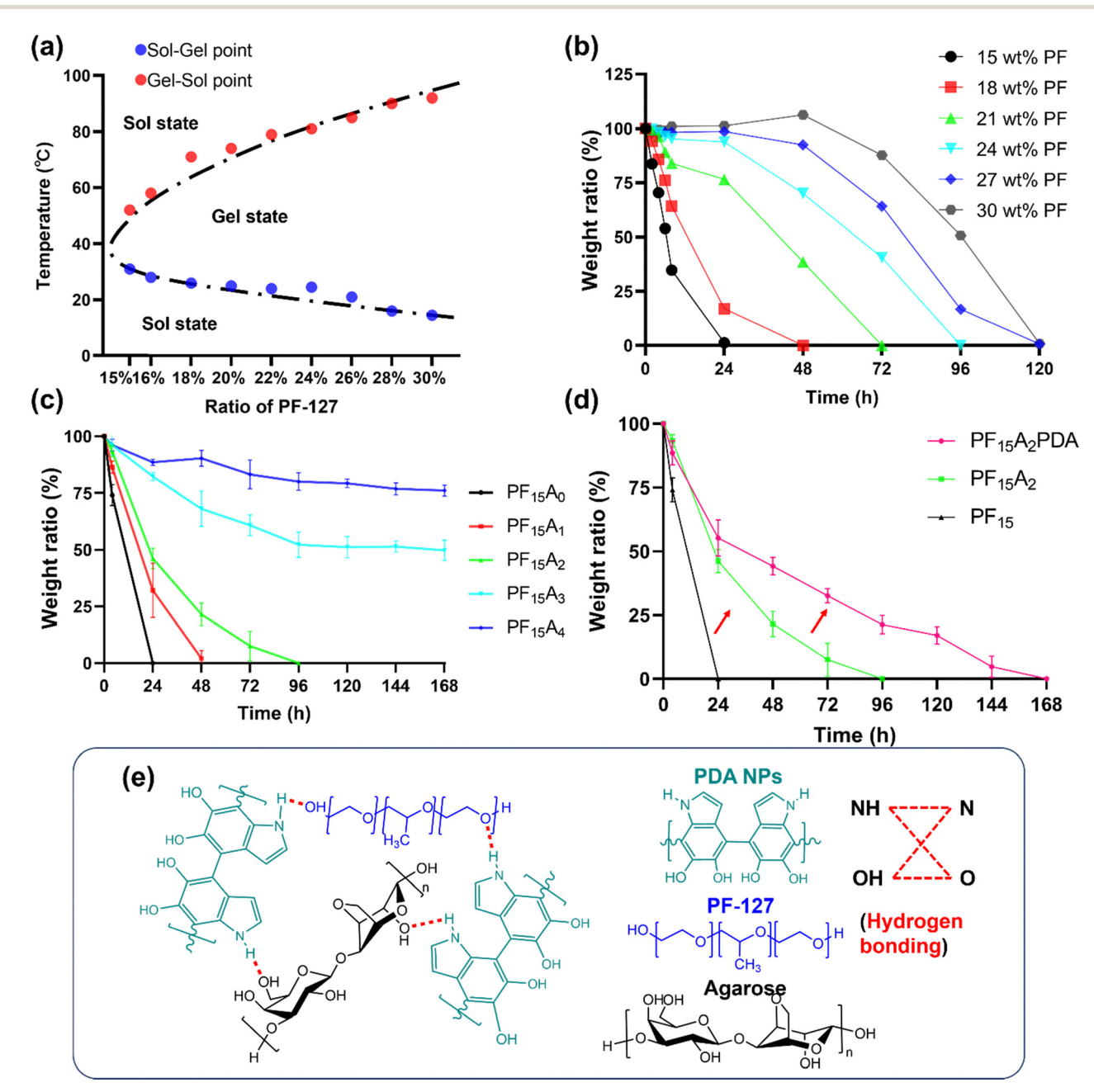


Fig. 3 Thermal transitions and degradation behavior of PF-based hydrogels. (a) Sol-gel and gel-sol points of the pure PF-127 hydrogel. (b) Degradation profile of the pure PF hydrogel at room temperature. (c) APF hydrogel degradation rate influenced by the ratio of agarose at room temperature. (d) Degradation profiles of the PF, APF composite, and PDA/APF composite hydrogels at room temperature. (e) Hydrogen bonding between PDA NPs and agarose or PF-127. (PF15A0: 15 wt% PF-127, 0 wt% agarose; PF15A1: 15 wt% PF-127, 1 wt% agarose; PF15A2: 15 wt% PF-127, 2 wt% agarose; PF15A3: 15 wt% PF-127, 3 wt% agarose; PF15A4: 15 wt% PF-127, 4 wt% agarose; PF15A2PDA: 15 wt% PF-127, 2 wt% agarose, 0.6 mg g<sup>-1</sup> PDA NPs).

completely within a day, which renders the PF hydrogel unsuitable for the intended application in this study. To address this, agarose polymers were incorporated into the composite hydrogel system to modulate the hydrophilic–hydrophobic balance and hydrogen-bonding interactions. This modification successfully prolonged the degradation period of the composite hydrogel, even at low PF-127 concentrations. Fig. 3c shows that the incorporation of 2 wt% agarose significantly prolonged the degradation period of the hydrogel system from less than 12 h to approximately 96 h. Notably, when the agarose content exceeded 3 wt%, phase separation occurred within the composite hydrogel system, leading to incomplete degradation. Therefore, the maximum agarose concentration used in the study was limited to 2 wt%.

Subsequently, PDA NPs were added to the APF composite hydrogel, which further prolonged its degradation period (Fig. 3d). This effect was attributed to the abundant N–H bonds and phenolic groups in the PDA NPs that participated in hydrogen-bonding interactions within the composite hydrogel, thereby enhancing its stability (Fig. 3e).

Notably, the incorporation of agarose and PDA NPs into PF-127 hydrogels led to a moderate increase in gel–sol transition temperatures, with PDA NPs exerting a more pronounced effect (Fig. S3, ESI†). This suggests that the addition of PDA NPs introduces a greater number of hydrogen bonding interactions, thereby further enhancing the physical strength of the hydrogel network. Moreover, it is important to note that increasing the transition temperature imposes limitations on the concentrations of the hydrogel components. For instance, the combination of 16 wt% PF-127, 1 wt% agarose, and 0.6 mg mL<sup>-1</sup> PDA NPs resulted in a Gel–Sol transition temperature as high as 66.6 °C. Such elevated temperatures can impair the hydrogel's NIR-triggered phase-transition capability.

# 2.3. Rheological, Fourier transform infrared spectroscopy (FTIR) characterization and Raman test of the composite hydrogel

Fig. 4a and b illustrate the changes in the storage and loss moduli of the PF, APF, and PDA/APF hydrogels over a temperature range of 15 °C to 75 °C. All three hydrogels exhibit significant changes in both moduli around 30 °C and 55 °C, indicating phase transitions from sol to gel and then back to sol state. In addition, the incorporation of agarose and PDA NPs expanded the gel-phase range of the hydrogels.

By identifying the points of maximum slope in the curves as the sol–gel and gel–sol transition temperatures, the sol–gel transition temperatures of the three hydrogels were determined to be 29.42  $^{\circ}$ C, 25.89  $^{\circ}$ C, and 25.31  $^{\circ}$ C, respectively, while the gel–sol transition temperatures were found to be 48.65  $^{\circ}$ C, 56.83  $^{\circ}$ C, and 58.99  $^{\circ}$ C, respectively. These results suggest that agarose and PDA NPs enhance the hydrogen bonding interactions within the PF-127 hydrogel network.

The FTIR spectra of the different hydrogels are shown in Fig. 4c and d. The absorption bands located at 1342 and 1360  $\rm cm^{-1}$  are attributed to the wagging motion of the -CH<sub>2</sub> group, whereas those appearing at 1242 and 1280  $\rm cm^{-1}$ 

correspond to twisting vibrations. Additionally, the stretching vibrations of the C–O–C bond manifest as three distinct peaks at 1147, 1112, and 1060 cm<sup>-1</sup>. Furthermore, the peak detected at 961 cm<sup>-1</sup> is associated with the rocking vibration of the –CH<sub>2</sub> group. <sup>46,51</sup> A characteristic peak at 2885 cm<sup>-1</sup> corresponds to the stretching vibration of the C–H bond. <sup>52</sup> Compared to the pure PF-127 hydrogel, the composite hydrogel containing agarose exhibits an additional characteristic peak at 934 cm<sup>-1</sup>, which can be attributed to the bending vibration of 3,6-anhydrogalactose. <sup>53</sup> Moreover, the –OH absorption band gradually shifted from 3525 cm<sup>-1</sup> and 3520 cm<sup>-1</sup> to 3516 cm<sup>-1</sup>, indicating the presence of hydrogen bonding interactions between agarose and PF-127. <sup>47</sup>

In this work, the Raman spectrum of pure PDA NPs exhibited two characteristic peaks at approximately 1340 cm<sup>-1</sup>, attributed to the C-N skeletal stretching vibration,54 and 1584 cm<sup>-1</sup>, corresponding to the aromatic C=C stretching vibration (Fig. 4e). 10 Upon encapsulation of PDA NPs within the APF hydrogel, both peaks underwent significant red shifts. Specifically, the C-N skeletal stretch shifted from 1340 to 1355 cm<sup>-1</sup> ( $\Delta = 15$  cm<sup>-1</sup>), and the aromatic C=C stretch shifted from 1584 to 1597 cm<sup>-1</sup> ( $\Delta = 13 \text{ cm}^{-1}$ ). These shifts are notably larger than those typically caused by weak van der Waals or  $\pi$ - $\pi$ interactions, thereby providing strong evidence for extensive hydrogen bonding between PDA NPs and the hydrogel matrix. The magnitude of these red shifts is consistent with literature reports and confirms that strong intermolecular hydrogen bonding interactions significantly influence the vibrational characteristics of PDA.

# 2.4. Structural characterization of the PF-127 and composite PDA/APF hydrogels

Fig. 5a shows SEM images of the dried PF-127 and PDA/APF hydrogels. Compared to the PF-127 hydrogel, the PDA/APF hydrogel exhibited smaller pore sizes (Fig. 5b), indicating a higher degree of crosslinking, likely due to stronger hydrogen bonding. Furthermore, the introduction of agarose and PDA NPs reduced the swelling ratio of the hydrogels (Fig. 5c), providing additional evidence of enhanced crosslinking in the composite hydrogel. The reduced swelling ratio of the APF hydrogel compared to the PF-127 hydrogel can be attributed to the formation of a denser and more robust polymer network. The incorporation of agarose introduces a secondary network structure, while PDA NPs enhance hydrogen bonding interactions with both agarose and PF-127. These additional physical crosslinks restrict the hydrogel matrix from expanding excessively when immersed in water, reducing its overall swelling capacity.

Fig. 5e shows the temperature variation in the PDA/APF hydrogel during NIR exposure. When subjected to NIR light at 2 W cm<sup>-2</sup>, the hydrogel's temperature rapidly increased from 30 °C to approximately 65 °C, then returned to approximately 30 °C within 5 min of cooling. This heating–cooling process, consisting of 5-min NIR irradiation followed by 5-min cooling, was repeated for five cycles. Throughout all the cycles, the temperature profile remained stable, indicating the excellent

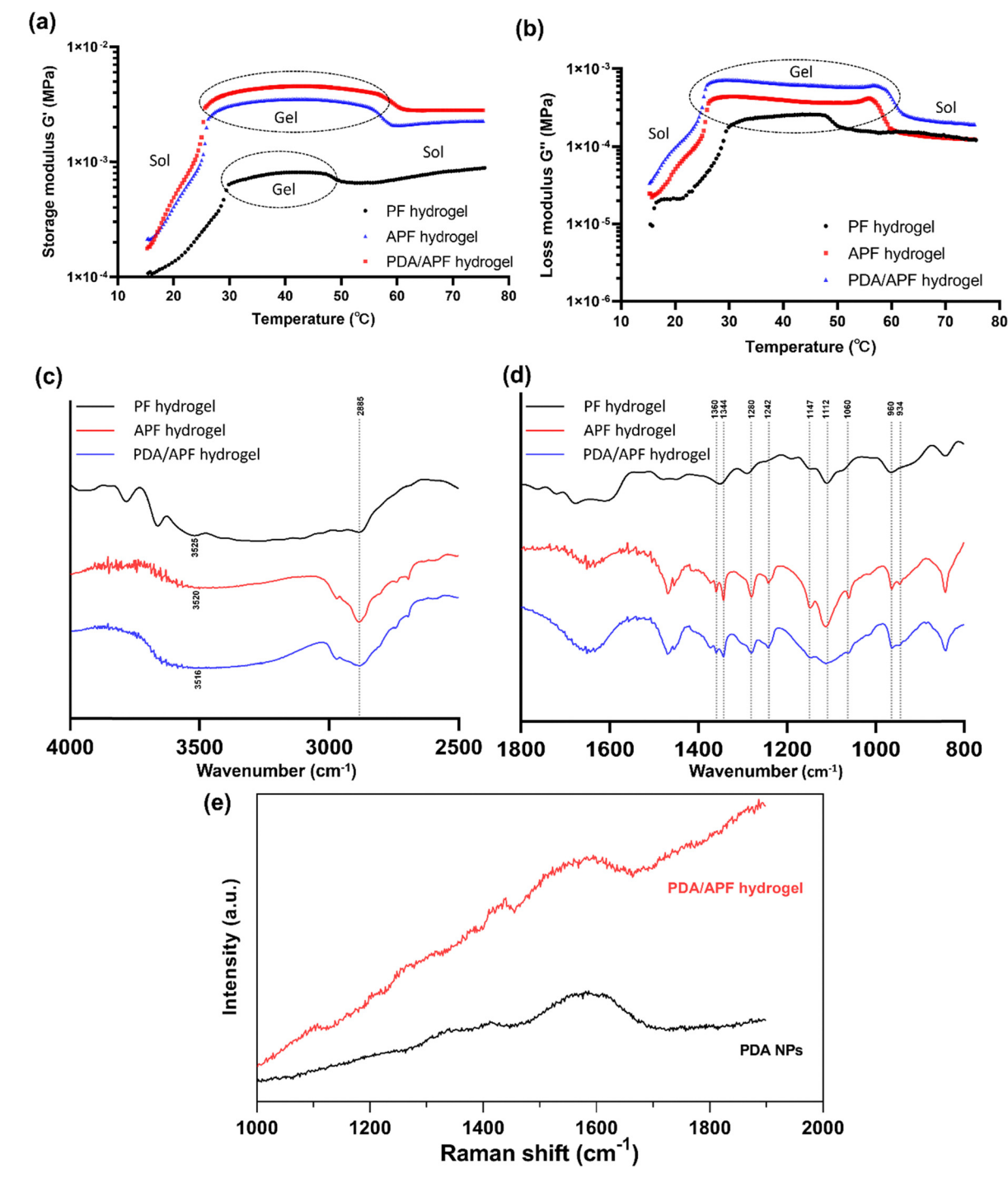


Fig. 4 Rheological measurements and Fourier transform infrared spectroscopy (FTIR) spectra of the PF, APF, and PDA/APF composite hydrogels. (a) Storage modulus of the hydrogels. (b) Loss modulus of the hydrogels. (c) FTIR spectra of the hydrogels in the 4000 cm<sup>-1</sup> to 2500 cm<sup>-1</sup> range. (d) FTIR spectra of hydrogels in the  $1800~{\rm cm}^{-1}$  to  $800~{\rm cm}^{-1}$  range, (e) Raman spectra of PDA NPs and PDA/APF hydrogel.

NIR-responsive property and stability of the PDA/APF composite hydrogel. The hydrogel also exhibits excellent flowability and injectability at room temperature (Fig. 5e). At 37 °C, it rapidly transitions into a gel state. When the hydrogel is maintained at a constant 37 °C and exposed to 808 nm laser irradiation, the APF composite hydrogel gradually softens and converts into a sol state within 5 minutes (Fig. 5f).

This transformation is reversible: once the environment cools down, the composite hydrogel returns to its non-flowable gel state.

#### 2.5. Drug releasing from PDA/APF hydrogel

Fig. 6a shows that the PDA/APF hydrogel underwent nearly complete degradation within 5 d, featuring a rapid degradation

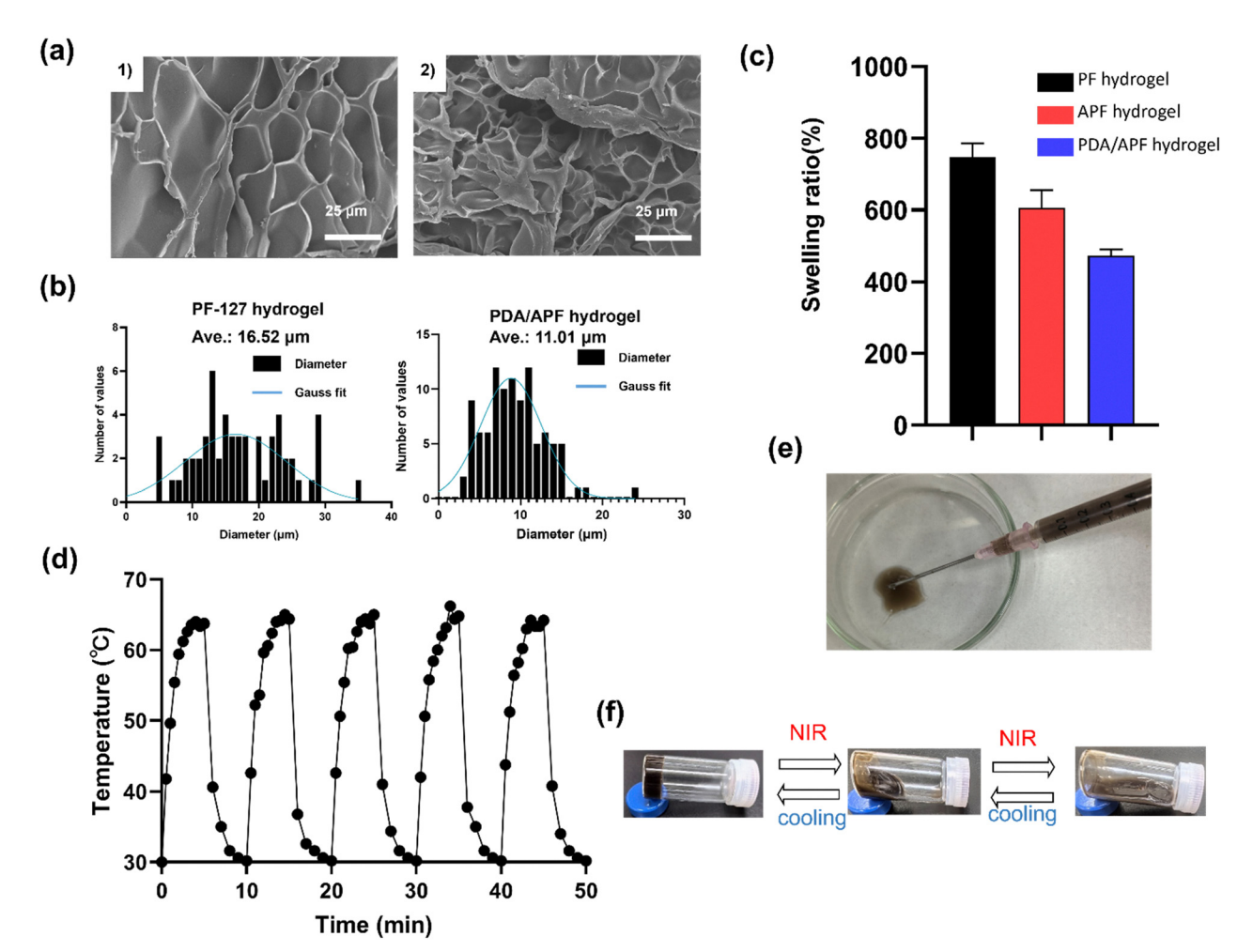


Fig. 5 Characterization of the composite hydrogels. (a) Scanning electron micrograph of the (1) PF-127 and (2) PDA/APF hydrogel. (b) Gaussian fit of pore size distribution and average pore size of the hydrogels. (c) Swelling ratio of hydrogels. (d) Temperature variation of PDA/APF hydrogel under a laser on/off cycle. (e) Demonstration of the injectability of the PDA/APF hydrogel. (f) NIR-responsive gel-sol transition of the PDA/APF hydrogel (laser on: 808 nm, 5 min, 4 W cm<sup>-2</sup>; laser off: 5 min).

phase in the first 8 h, followed by a slower rate thereafter. This trend aligns well with that of previous research findings. Compared to the hydrogel containing 15 wt% PF-127, which degrades within 12 h, the incorporation of PDA NPs and 2 wt% agarose successfully prolonged the degradation period to over 5 d. This suggests that additional hydrogen bonding and increased crosslinking enhanced the stability of the hydrogel network, making it more suitable for sustained drug delivery applications.

SN-38, the active metabolite of irinotecan, has a structural and pharmacokinetic profile similar to that of its parent compound. Because both SN-38-chol and SN-38-chol NPs (prodrug) are lipophilic, they are not ideal for accurately simulating drug release from the hydrogel. Therefore, irinotecan, which is hydrophilic, was selected as the control for hydrogel release experiments.<sup>55</sup> Fig. 6b shows the release profiles of SN-38-chol NPs and irinotecan from the PDA/APF hydrogel. Irinotecan was released at a faster rate than SN-38-chol NPs, with over 80% released within 24 h and complete release within 2 d. In contrast, SN-38-chol NPs exhibited a

relatively faster release in the first 24 h, followed by a more gradual and sustained release over the next 4 d, which closely correlated with the degradation curve of the hydrogel.

To further explore the relationship between hydrogel degradation and drug release, the cumulative percentage of drug release was plotted against the hydrogel degradation ratio. The results indicated that the release profile of SN-38-chol NPs followed a linear trend, whereas that of irinotecan exhibited a quadratic increase (Fig. 6c). The difference in release behaviour is illustrated in Fig. S4 (ESI†). Due to the larger particle size of SN-38-chol NPs, their diffusion through the hydrogel network was restricted, making their release primarily dependent on hydrogel degradation. In contrast, irinotecan, which is a small-molecule drug, is not significantly hindered by the hydrogel network and can be released through both hydrogel degradation and free diffusion, resulting in a significantly faster release profile than that of the SN-38-chol NPs.

The results of NIR-triggered release behaviour of SN-38-chol NPs from the APF hydrogel were shown in Fig. 6d. In the experimental setup, 1 mL of hydrogel was placed at the bottom

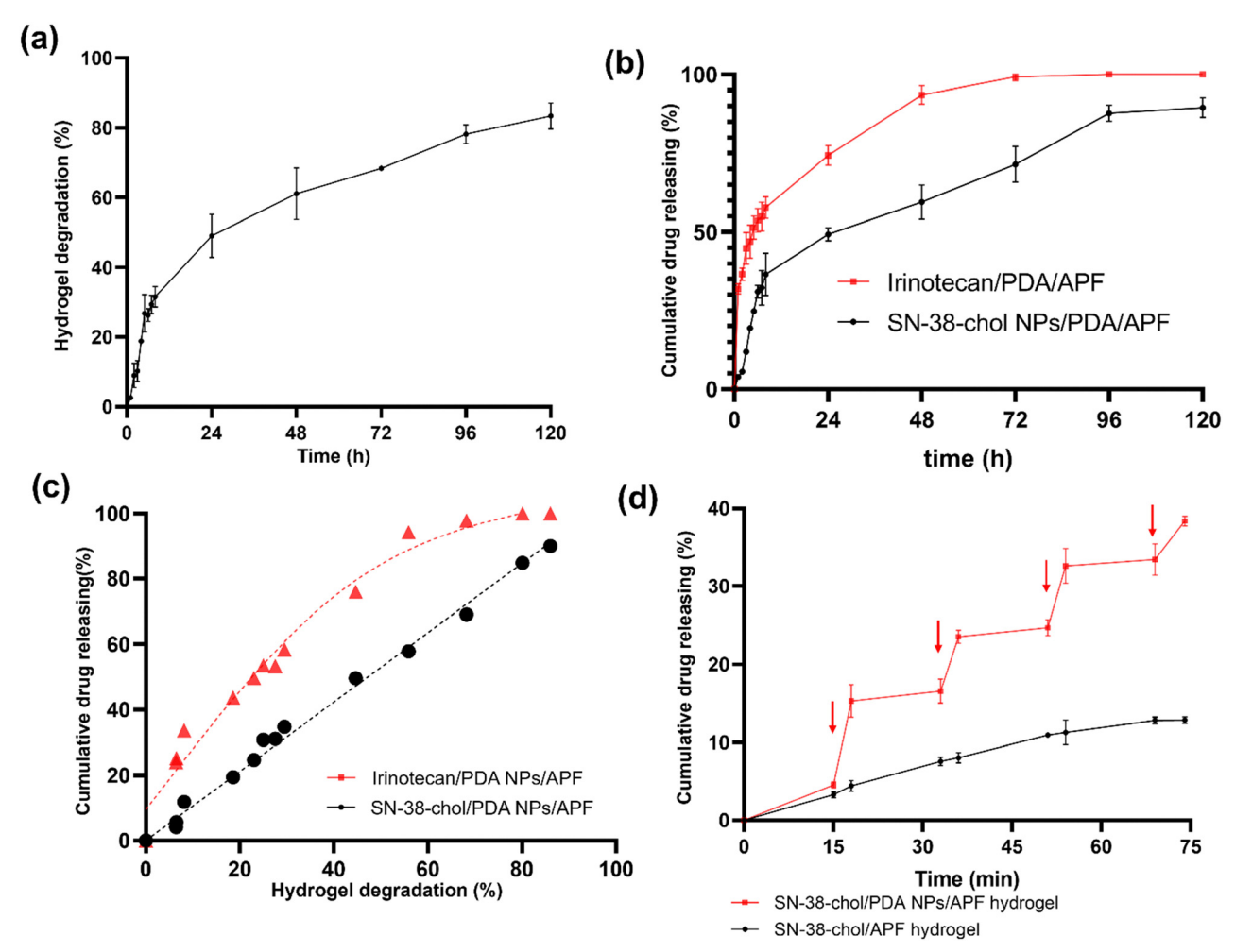


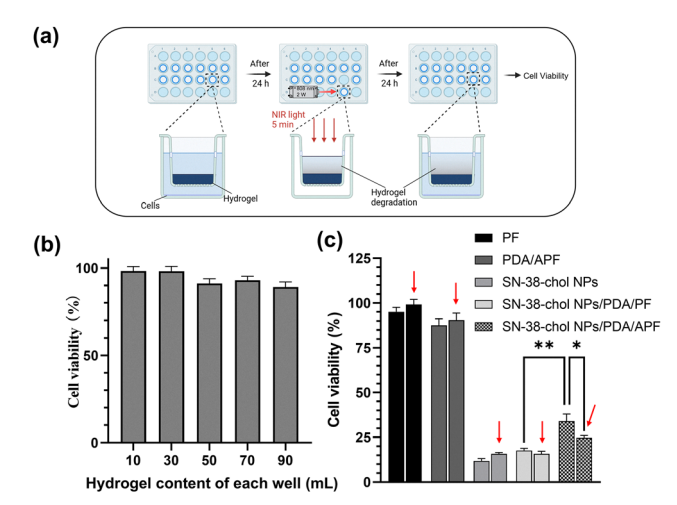
Fig. 6 Hydrogel degradation and drug release. (a) Degradation of PDA/APF hydrogel. (b) Cumulative drug release of irinotecan and SN-38-chol NPs from the PDA/APF hydrogel. (c) Drug release curve of irinotecan and SN-38-chol according to the hydrogel degradation ratio. (d) NIR-responsive drug release from APF hydrogel. Red arrow: NIR irradiation (3 min, 4 W cm $^{-2}$ , 808 nm). Data are presented as mean  $\pm$  standard deviation (n = 3).

of a vial containing 3 mL of deionized water. To initiate drug release, the hydrogel was irradiated with 808 nm NIR light for 3 minutes at 15-minute intervals (red arrows in Fig. 6d). The vial was placed on a 50 °C heating plate to maintain the initial temperature of both the hydrogel and surrounding solution at approximately 37 °C. To minimize the heat-buffering effect of water due to its high specific heat capacity, the vial was laid on its side before each NIR irradiation to ensure that the hydrogel was only partially submerged in water. NIR light was then applied to the exposed upper portion of the hydrogel to induce partial melting. After irradiation, the vial was returned to an upright position to allow released drug to dissolve into the water. The concentration of SN-38-chol NPs in the solution was then quantified by UV-vis spectroscopy. The results show that NIR irradiation had little effect on the release of SN-38-chol NPs from hydrogels without PDA NPs. In contrast, the PDA NPsloaded APF hydrogel exhibited rapid drug release after each 3minute NIR irradiation. These findings indicate that the incorporation of PDA NPs imparts excellent NIR-responsive drug release capability to the hydrogel. Therefore, the SN-38-chol/ PDA NPs/APF hydrogel system demonstrates strong potential as a controlled drug delivery carrier for in vivo applications.

#### 2.6 Cytotoxicity assay

For the *in vitro* experiments, a 24-well co-culture plate was used as the cultivation platform. HCT-116 cells were seeded in the lower layer, and the hydrogel was injected into the upper chambers. The chambers were equipped with a 0.45 µm filter membrane, allowing released SN-38-chol NPs to pass through while retaining the non-hydrolyzed hydrogel.

To simulate hydrogel degradation and drug release under NIR light while preventing direct and indirect cell damage from irradiation and photothermal effects, the chambers were relocated to different positions on the plate after 24 h of culture. They were then irradiated with NIR light (808 nm, 4 W cm<sup>-2</sup>) for 5 min before being returned to their original positions (Fig. 7a). The dark gray hydrogel hydrolyzed and diffused after irradiation, confirming that the NIR-induced temperature elevation successfully triggered the gel-sol transition, leading to hydrogel degradation.



Cytotoxicity of the hydrogel. (a) Schematic illustration of the coculture design for hydrogels and cells. (b) Cell viability after treatment with blank PDA/APF hydrogels at concentrations ranging from 10 µL to 90 µL per well. (c) Cell viability after treatment with drug-loaded and blank hydrogels (drug content =  $0.28 \mu mol \ mL^{-1}$ , hydrogel content =  $50 \mu L \ per$ well). Data are presented as mean  $\pm$  standard deviation (n = 3, \*P < 0.05, \*\*P < 0.01). Cell line: HCT-116 human colon cancer. Red arrows: NIR irradiation (5 min, 4 W cm<sup>-2</sup>, 808 nm).

Fig. 7b shows the viability of HCT-116 cells treated with the PDA/APF hydrogel at varying concentrations without drug loading. The results indicate nearly 100% cell viability, demonstrating the low toxicity of the blank hydrogel. Fig. 7c shows the viability of cells treated with different hydrogels. The results revealed that the PF and PDA/APF hydrogels exhibited minimal toxicity, whereas the drug-loaded hydrogels induced similar cytotoxicity to an equivalent dose of SN-38-chol NPs.

Owing to the rapid degradation of the PF hydrogel, which almost fully decomposed within 48 h, its drug-loaded form exhibited cytotoxicity comparable to that of the SN-38-chol NPs, regardless of NIR irradiation. In contrast, the PDA/APF hydrogel degraded more slowly, leading to higher cell viability compared to the PF hydrogel. However, NIR irradiation accelerated PDA/APF hydrogel degradation and enhanced the release of SN-38-chol NPs, significantly increasing the cytotoxicity in the SN-38-chol/PDA/APF + NIR group. This further confirmed that NIR light effectively promoted hydrogel degradation and drug release.

#### 2.7. *In vivo* therapy

Based on the excellent NIR-responsive sol-gel transition of the SN-38-chol/PDA/APF hydrogel system observed in vitro and the demonstrated antitumor potential and NIR-induced cytotoxicity in cell experiments, we further evaluated its in vivo efficacy using a BALB/c nude mouse model implanted with HCT-116 colon cancer cells.

As illustrated in Fig. 8a, the hydrogel was injected in its sol state into the tumor site at room temperature on days 7 and 17 after tumor implantation. Three days after hydrogel injection, NIR irradiation was applied to the tumor site to trigger PTT and induce the gel-sol transition, thereby releasing the loaded drug

NPs. The 30 mice were divided into six groups, with five mice per group: G1 (control group, no treatment), G2 (PF hydrogel loaded with SN-38-chol NPs), G3 (APF hydrogel loaded with SN-38-chol NPs), G4 (APF hydrogel loaded with PDA NPs + NIR), G5 (APF hydrogel co-loaded with irinotecan and PDA NPs + NIR), and G6 (APF hydrogel co-loaded with SN-38-chol and PDA NPs + NIR). Groups G4, G5, and G6 received the NIR-assisted treatment.

Fig. 8b shows the in vivo NIR-induced mice body temperature change, and the body temperature of anesthetized mice initially drops to approximately 32 °C. After 5 min of NIR irradiation, the tumor temperature in the SN-38-chol/PDA/APF group rapidly increased from 32.9 °C to 64.4 °C within 2 min and remained stable at around 65 °C for approximately 3 min (Fig. 8b), indicating the excellent NIR responsiveness of the hydrogel in vivo. On contrast, PDA NPs-free hydrogel didn't show significant temperature change. Fig. 8c presents the temperature distribution of the tumor site after 5 min of NIR irradiation.

Fig. 8d shows the relative changes in the tumor size during the treatment period. Compared with the control group, the SN-38-chol/PF group showed no significant difference in tumor growth. During the first 14 days, the therapeutic effect in the SN-38-chol NP/PF group was similar to that in the APF group. However, in the last seven days, tumor growth accelerated, indicating that owing to the rapid degradation of the PF-127 hydrogel, its long-term drug release was insufficient over the 21-day treatment period, making it unsuitable as a sustained drug delivery carrier. The SN-38-chol NPs group (chemotherapy group), PDA NPs group (PTT group), and irinotecan + PDA NPs group (combination therapy group) showed significant tumor suppression compared with the control group, demonstrating that both chemotherapy and PTT exhibited tumor-killing effects. However, the incorporation of irinotecan into the hydrogel system did not enhance tumor cytotoxicity, suggesting that irinotecan exhibited limited long-term tumor-killing effects in vivo due to its rapid release rate. In contrast, the SN-38-chol NPs + PDA NPs + NIR group exhibited the most potent tumor suppression. The tumor was almost completely eradicated within 21 d of treatment, indicating that SN-38-chol NPs, with their slower release rate, hold greater therapeutic potential than irinotecan in long-term tumor treatment.

Fig. 8e shows the tumor images after 21 d of treatment. In the combination therapy group (G6), three out of five mice achieved complete tumor eradication, with no visible masses or hard lumps at the tumor implantation site. Among them, one mouse still had an unhealed wound, likely due to an open lesion left by tumor ablation, which was expected to heal over time. Fig. 8f illustrates the absolute tumor size in each group. In G6 (SN-38-chol NPs/PDA/APF + NIR), two mice exhibited complete tumor regression by day 14, another mouse by day 17, and the remaining two mice showed significant tumor shrinkage, further confirming the superior tumor-killing efficacy of the NP-mediated combination therapy with PTT. Finally, Fig. 8g compares the tumor weights post-dissection, which is consistent with the previously described results. The average tumor

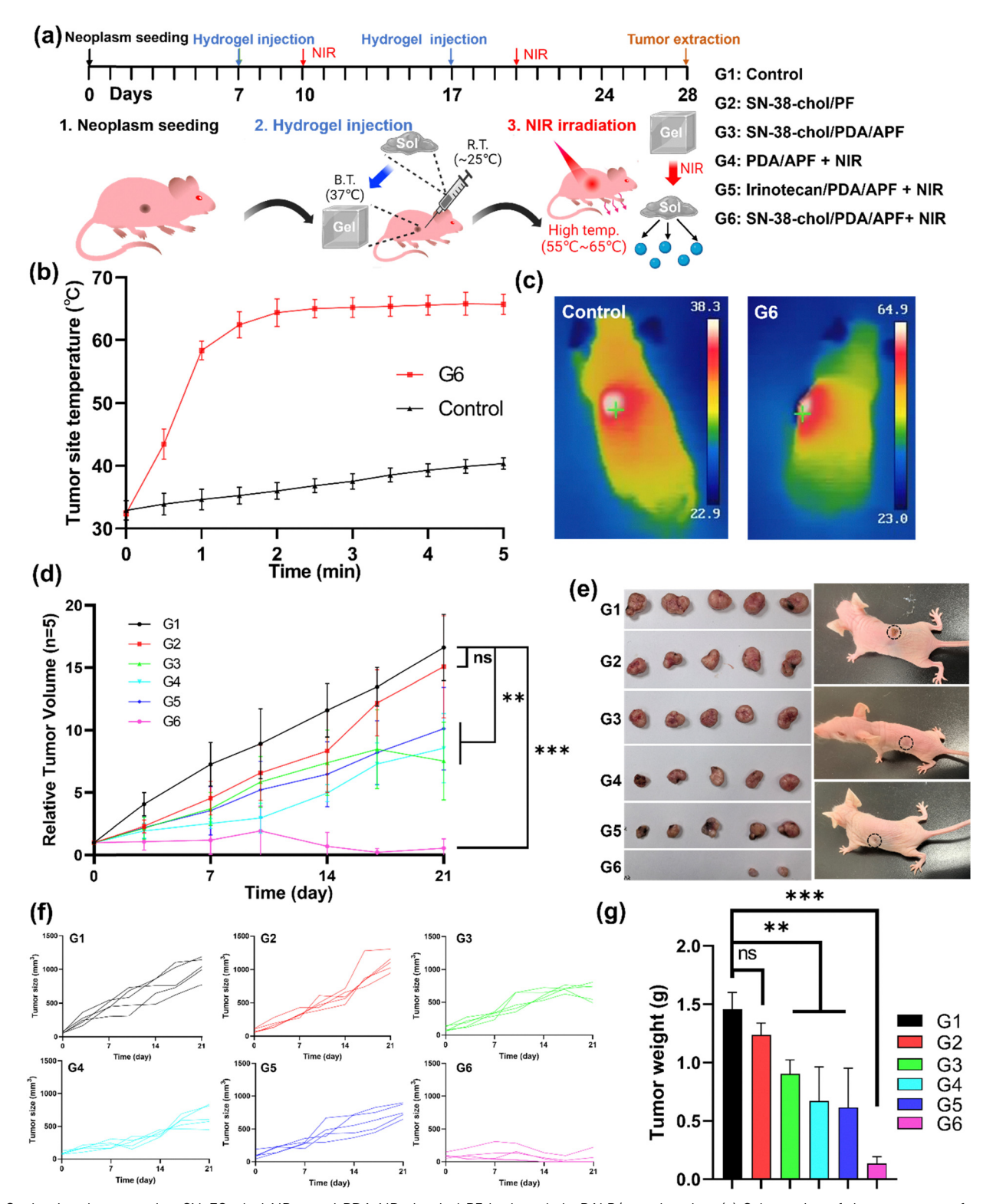


Fig. 8 In vivo therapy using SN-38-chol NPs- and PDA NPs-loaded PF hydrogels in BALB/c nude mice. (a) Schematics of the treatment of tumorbearing mice. (b) Temperature change for 5 min at the NIR-irradiated site. (c) Thermograph of hydrogel irradiated by NIR light after 5 mins. Left panel: Control group, right panel: SN-38-chol/PDA/APF group. (d) Tumor growth curves after implantation of SN-38-cholesterol NPs-loaded hydrogels under different treatments. (e) Pictures of the extracted tumors, (f) tumor size, and (g) tumor weight in the different treatment groups. (G1 (control), G2 (SN-38chol NPs/PF-127 hydrogel), G3 (SN-38-chol NPs/APF hydrogel), G4 (PDA NPs/APF hydrogel + NIR), G5 (irinotecan/PDA NPs/APF hydrogel + NIR), and G6 (SN-38-chol NPs/PDA NPs/APF hydrogel + NIR)). Data is presented as means  $\pm$  standard deviation (n = 5, \*\*P < 0.01, \*\*\*P < 0.001).

weight in the control group was 1.456 g, while in the G6 group, the average tumor weight was 0.1337 g. This indicates that three mice in the G6 group had complete tumor ablation, while the remaining two showed about 91% ablation.

#### 2.8. Side effects

Fig. 9a illustrates the changes in the body weight of mice during the treatment process. Overall, there were no significant differences in body weight among the groups; however, mice in the treatment groups exhibited slightly lower body weights, indicating that chemotherapy or PTT had some adverse effects.

Fig. 9b shows the red blood cell (RBC) count. Compared with the control group, RBC counts increased in groups G3, G4, G5, and G6, where tumor reduction was observed. This suggests successful recovery of hematopoietic function in the mice after treatment.

Fig. 9c shows the white blood cell (WBC) counts. Compared with the control group, the WBC count was higher in groups G3 and G6, which underwent chemotherapy, and lower in groups G4 and G5, which received PTT. This may be attributed to PTT-induced immune cell depletion and migration, whereas chemotherapy has been reported to reactivate immune cells, thereby increasing the WBC count. Consequently, a significant increase in WBC count was observed in the G6 group under the combined therapy, suggesting immune system reconstruction and activation in mice. Overall, under the combined treatment with SN-38-chol NPs and PDA-mediated PTT, the mice experienced a slight decrease in body weight, while both WBC and RBC counts noticeably increased. These results indicate that the adverse effects of the combination therapy in mice were relatively mild, highlighting its potential clinical significance.

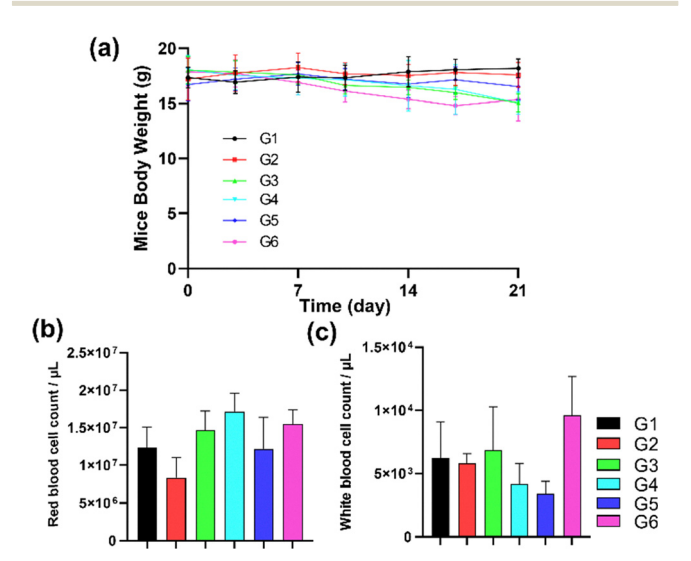


Fig. 9 Side effects of the hydrogel treatment. (a) Changes in the body weight of mice receiving various treatments. (b) Red blood cell and (c) white blood cell count of mice receiving various treatments. (G1 (control), G2 (SN-38-chol NPs/PF-127 hydrogel), G3 (SN-38-chol NPs/PDA NPs/APF hydrogel), G4 (PDA NPs/APF hydrogel + NIR), G5 (irinotecan/PDA NPs/APF hydrogel + NIR), and G6 (SN-38-chol NPs/PDA NPs/APF hydrogel + NIR)). Data is represented as means  $\pm$  standard deviation (n = 5).

#### Discussion and conclusion

In this study, we explored the NIR-responsive drug release of a novel composite PDA/APF hydrogel. Pure PF-127 hydrogels achieved a prolonged degradation period only at high concentrations. However, this significantly raised the gel–sol transition temperature above 80 °C, which is not suitable for clinical applications. Considering that the low mechanical strength of the PF-127 hydrogel limits its application in drug delivery and that chemical modification of the PF-127 backbone or the use of crosslinking agents could increase the toxicity of the hydrogel system, this study attempted to incorporate biocompatible agarose polymers as a secondary network within the hydrogel system. Additionally, the hydroxyl- and amine-rich characteristics of the agarose- and NIR-responsive PDA NPs were utilized to enhance hydrogen bonding within the PF-127 hydrogel, thereby improving its mechanical strength.

To further enhance the application of this hydrogel system, SN-38-chol NPs were selected as drug-loading NPs due to their nearly 100% drug-loading efficiency and exceptional stability, making them promising anticancer agents.<sup>24</sup> SN-38-chol NPs were incorporated into a PDA/APF hydrogel to improve the drug release performance of the composite hydrogel system. Compared with traditional molecular drugs, pure drug NCs offer unique advantages. First, drug NCs eliminate the need for a carrier, thus mitigating the toxicity and side effects associated with the excipients used for solubilization.<sup>57</sup> Second, drug NCs have a loading rate close to 100% and are entirely composed of drug molecules. 18 Third, release rate from hydrogel systems of drug NCs is lower than molecular drugs.58 In this study, the SN-38-chol NPs demonstrated stability for several weeks, exhibited a small size, and did not require additional surfactants, thus establishing them as excellent anticancer drugs.

Experimental results demonstrated that PDA/APF composite hydrogel system exhibited excellent sol–gel–sol transition properties, with gelation and dissolution temperatures of 25.3  $^{\circ}$ C and 59.0  $^{\circ}$ C, respectively, which allowed for controlled drug release upon NIR-induced temperature elevation. Additionally, compared with the pure PF-127 hydrogel, this system significantly prolonged the degradation period from <1 d to >7 d, ensuring sustained drug delivery.

In vitro experiments confirmed that the PDA/APF hydrogel effectively released SN-38-chol NPs and enhanced their cytotoxicity under NIR irradiation, thereby achieving synergistic anticancer effects. We demonstrated the *in vivo* efficacy of the PDA/APF hydrogel system through comprehensive animal experiments. BALB/c nude mice bearing subcutaneous HCT 116 tumors were treated with different hydrogel formulations, and therapeutic outcomes were assessed by monitoring tumor growth, body weight, and hematological parameters. Tumor volume measurements indicated that mice treated with the SN-38-chol/PDA/APF hydrogel (G6 group) exhibited the most significant tumor suppression compared to other groups. In the G6 group, three mice had complete tumor ablation, while the remaining two showed about 91% ablation, with tumor sizes significantly smaller than those in the control

and single-treatment groups. This confirmed that the integration of drug-loaded hydrogels with PTT enhanced anticancer efficacy through a synergistic mechanism. However, further histological analysis and prolonged observation will be necessary to comprehensively evaluate therapeutic efficacy and potential recurrence.

This study presents a novel injectable, NIR-responsive hydrogel system with promising applications in tumor chemotherapy and photothermal therapy. Compared to other hydrogel-based drug delivery systems, our design emphasizes the use of biocompatible, naturally derived materials to reduce potential toxicity risks associated with chemical modification.<sup>59</sup> While many existing systems depend on chemical crosslinkers or synthetic polymers to improve mechanical strength or responsiveness,60,61 our strategy utilizes the intrinsic gel-sol transition behavior of PF127 combined with agarose to construct a physically crosslinked dual-network hydrogel. This approach enhances the hydrogel's structural integrity while retaining excellent injectability and NIR-responsiveness. By enhancing hydrogen bonding interactions within the hydrogel network, we successfully maintained the low gel-sol transition temperature of the composite hydrogel while extending its degradation period. This improvement enables the PF127based hydrogel to serve as a suitable platform for PDA NPsmediated, NIR-responsive photo-chemo drug delivery.

As such, our system offers a distinct and complementary alternative to existing controlled-release platforms. The injectable and thermally reversible nature of the PDA NPs/APF hydrogel makes it a promising candidate for advanced biomedical applications such as 3D-bioprinted tissue scaffolds and self-healing drug depots. <sup>62,63</sup> These future directions could extend its use beyond oncology into wound healing, regenerative medicine, and personalized therapeutic delivery.

#### 4. Materials and methods

#### 4.1 Preparation of SN-38-chol NPs

SN-38-chol NPs were prepared by a reprecipitation method using two distinct concentration formulations. For the 0.1 mM nanoparticle synthesis, a THF solution containing 0.861 mg SN-38-chol (100  $\mu L)$  was rapidly injected into 9.9 mL of vigorously stirred aqueous solution using a microsyringe, completing the injection within 5 seconds. The higher concentration variant (0.4 mM) was prepared by injecting 200  $\mu L$  of THF solution containing 1.722 mg SN-38-chol into 4.8 mL of water under identical mixing conditions.

The particle size distribution and PdI of the fabricated SN-38-chol NPs were assessed through DLS measurements conducted on a Malvern Zetasizer NanoZS system. Furthermore, morphological features were examined by scanning electron microscopy (SEM) using a Hitachi S-4800, providing high-resolution imaging of nanoscale structures.

#### 4.2. Preparation of PDA NPs

PDA NPs were fabricated *via* oxidative self-polymerization in a dispersion-mediated synthesis system.<sup>58</sup> The protocol commenced

with mixing 4 mL ethanol and 9 mL deionized water containing 0.1 mL ammonia solution (25% v/v) under continuous magnetic agitation at 25 °C. Dopamine (DA) precursor solution was prepared by dissolving 0.05 g powdered DA in 1 mL aqueous medium, which was subsequently introduced into the reaction mixture. Polymerization proceeded under light-excluded conditions with sustained stirring over 40 h. Purification after synthesis was performed by three rounds of centrifugation  $(12\,000 \times g, 15\,\text{min})$  with deionized water to remove impurities. Nanoparticle yield was determined through gravimetric quantification after vacuum desiccation, followed by aqueous redispersion. PDA NPs were stored in deionized water after preparation and subjected to ultrasonic resuspend for redispersion before use. Particle size distribution and PdI were evaluated by DLS, with morphological analysis conducted via SEM imaging.

#### 4.3. Preparation of composite hydrogel

First, PF-127 hydrogel was prepared by dissolving different amounts of PF-127 powder in deionized water, followed by incubation at 95 °C for 30 minutes to form hydrogels with different concentrations. To fabricate the agarose & PF-127 composite hydrogel (APF hydrogel), agarose powder and PF-127 powder were thoroughly mixed before being added to deionized water. The mixture was then rapidly stirred in a 95 °C water bath until a homogeneous solution was formed. After cooling to room temperature, the APF composite hydrogel was successfully obtained. According to experimental requirements, the agarose concentration was set at 1 wt%, 2 wt%, 3 wt%, and 4 wt%, while the PF-127 concentration was fixed at 15 wt%. The prepared hydrogel was stored in its gel state at 37 °C to prevent phase separation.

PDA NPs-incorporated hydrogel was obtained by simply adding different amounts of 1.2 mg mL<sup>-1</sup> PDA NPs solution before hydrogel formation. By adjusting the volume of the PDA NPs solution, hydrogels with varying PDA NPs concentrations can be easily prepared.

#### 4.4. Characteristics of hydrogel systems

**4.4.1. Measurement of gel-sol-gel point.** The inverted vial method was used to analyze the gel-sol-gel transition points of PF-127 hydrogel and APF hydrogel at different weight percentages. 1 mL sol-state hydrogel, pre-cooled to 4 °C, was injected into a 5 mL vial and then gradually warmed to room temperature. The average temperature of the hydrogel was monitored using a thermography camera (E1L, Hikmicro). Once the hydrogel reached room temperature, it was further heated from 20 °C to 90 °C using a water bath. During this heating process, the morphological changes of the hydrogel were observed. The transition from sol to gel was determined when the hydrogel ceased gravitational flow (as assessed by the inverted vial method), while the transition from gel back to sol was identified when gravitational flow reappeared.

**4.4.2. Hydrogel degradation.** A 1 mL sample of either PF-127 hydrogel or APF hydrogel at different concentrations was added to 5 mL of PBS solution and incubated for 7 days.

At specific time points, the PBS solution was removed, and the hydrogel was freeze-dried. The weight of the dried vial was measured as M1, while the initial weight of the empty vial was previously determined as M. The freeze-dried weight of 1 mL of hydrogel was recorded as M0. The degradation rate of the hydrogel was calculated using the following formula:

Hydrogel weight ratio (%) =  $(M1 - M)/M0 \times 100\%$ 

Hydrogel degradation (%) =  $(1 - (M1 - M)/M0) \times 100\%$ 

- **4.4.3. Rheological test.** The rheological characteristics of the hydrogels were analyzed using a rotational rheometer (Waters, HR-20). The samples were positioned in a 1.2 mm gap between the measuring plates at a fixed oscillation frequency of 1 Hz. The temperature was increased gradually from 15 °C to 75 °C to monitor changes in the storage and loss moduli of the hydrogels.
- **4.4.4. FTIR.** The FTIR spectra were acquired using a spectrometer (Thermo Fisher, Nicolet iS20). Measurements were carried out on samples of agarose, PF127, and APF hydrogels, with the spectral range set from 4000 to 400 cm<sup>-1</sup>.
- **4.4.5. SEM.** The hydrogel's porous structure was characterized using SEM following a standardized sample preparation protocol. Prior to microscopic evaluation, hydrogel specimens underwent cryogenic preservation through lyophilization  $(-50~^\circ\text{C}, 24~\text{h})$  to maintain structural integrity during dehydration. The desiccated matrices were then precision-sectioned into 0.5-mm-thick lamellae. Mounting procedures involved securing the cross-sectional surfaces to aluminum stubs with carbon tape, ensuring optimal electrical conductivity. To enhance surface charge dissipation, a 5 nm platinum coating was deposited via magnetron sputtering prior to SEM imaging at 5 kV accelerating voltage.
- **4.4.6. Swelling ratio.** The equilibrium swelling behaviour was assessed using gravimetric analysis. Lyophilized specimens of PF-127, APF, and PDA NPs/APF composites were precisely weighed  $(W_d)$  and hydrated under controlled conditions in deionized water at room temperature. After 5 days of immersion with the solution refreshed daily, the swollen samples were weighed  $(W_s)$  after carefully removing excess water. The swelling ratio (%) was calculated as:

Swelling ratio (%) =  $(W_s - W_d)/W_d \times 100\%$ 

4.4.7. NIR-responsive property. To investigate the thermal reversibility and NIR-responsive property of the PDA NPs/APF hydrogels, the hydrogels underwent multiple cycles of NIR irradiation and cooling. During each cycle, the hydrogels were exposed to 808 nm NIR light at a power density of 4 W cm<sup>-2</sup> for 5 minutes at fixed position. The initial temperature of the hydrogel before irradiation was recorded. After irradiation, the laser was turned off, and the hydrogels were allowed to cool to room temperature for 5 minutes. The hydrogel specimen was prepared as a cylinder with a diameter of 2 cm and a height of 0.5 cm. The temperature during NIR irradiation was recorded using an infrared thermal camera, and the maximum

temperature detected on the hydrogel surface was used for analysis.

**4.4.8.** Raman test. Raman spectra were recorded using a confocal Raman microscope (inVia/Renishaw) equipped with a 532 nm laser as the excitation source. The laser power was set to 5 mW to avoid sample damage. A  $50\times$  objective lens was used to focus the laser onto the sample surface. The integration time for each spectrum was 0.5 seconds, and measurements were performed on both PDA NPs and PDA-incorporated composite APF hydrogels. All spectra were baseline-corrected before analysis.

#### 4.5. Drug loading and drug release

Drug-loaded hydrogels were prepared by incorporating SN-38-chol NPs or irinotecan solution before hydrogel formation. Specifically, 0.4 mM SN-38-chol NPs or irinotecan solution was mixed with PF-127 powder or pre-blended agarose & PF-127, followed by the addition of 1.2 mg mL $^{-1}$  PDA NPs. The mixture was then rapidly stirred and heated in a 95  $^{\circ}\text{C}$  water bath to form the drug-loaded hydrogel. Using this method, irinotecan/PDA NPs/APF hydrogel, SN-38-chol/PDA NPs/APF hydrogel, and SN-38-chol/PDA NPs/PF-127 hydrogel were successfully prepared, each with a drug loading concentration of 0.312  $\mu\text{mol mL}^{-1}$ .

To evaluate drug release, 1 mL of each hydrogel was placed in 5 mL of PBS, allowing the drug to diffuse over time. At specific intervals over five days, samples were collected, and the concentration of released SN-38-chol NPs or irinotecan was measured using liquid chromatography-mass spectrometry (LC-MS; Agilent 1260 Infinity, Agilent Technologies, Santa Clara). The cumulative drug release percentage was then calculated.

#### 4.6. Cell culture and treatments

Cytotoxicity was assessed using an in vitro assay with the HCT-116 human colon cancer cell line, sourced from the Riken Cell Bank. The cells were maintained in Dulbecco's Modified Eagle's Medium (DMEM) supplemented with 10% fetal bovine serum at 37 °C in a humidified incubator with 5% CO<sub>2</sub>. In order to co-culture hydrogels with cells without affecting cell growth, a 24-well co-culture plate (Corning 3473) was used as the culture platform in this study. HCT-116 cells were seeded in the lower layer, while the hydrogel was injected into the upper chambers. The chambers were equipped with a 0.45 µm filter membrane, allowing released SN-38-chol NPs to pass through while retaining the non-hydrolyzed hydrogel. To simulate hydrogel degradation and drug release under NIR light while preventing direct and indirect cell damage from irradiation and photothermal effects, the chambers were relocated to a different position in the plate after 24 hours of culture. They were then irradiated with NIR light (808 nm, 4 W cm $^{-2}$ ) for 5 minutes before being returned to their original position (Fig. 7a). The cell concentration in the medium of each well was measured using a Cell Counting Kit-8 (CCK-8; DOJINDO).

#### 4.7. Animal experimentation and in vivo hydrogel injection

The Ethical Committee of the Graduate School of Medicine, Tohoku University, approved the protocol under no. 2019MdA001.

The methods were carried out in accordance with the approved guidelines.

All animals were randomly assigned to experimental groups using a random number generator to minimize selection bias. During treatment administration and data collection, the investigators were blinded to group assignments to reduce observational bias. Data analysis was also conducted in a blinded manner to ensure objectivity and reproducibility of the results.

Female BALB/c nude mice (6 weeks old) were obtained from Charles River Laboratories, Japan, and housed under controlled environmental conditions, maintaining a temperature of 22  $\pm$ 4 °C and humidity of 50  $\pm$  10%, with a natural light/dark cycle. After a one-week acclimatization period, each mouse was subcutaneously injected with 100 µL of an HCT-116 cell suspension  $(1 \times 10^7 \text{ cells per mL})$  into the flank under anesthesia. Tumor growth was monitored, and treatment began once the tumor diameter reached 5-7 mm.

On days 7 and 17 post-inoculation, drug-loaded hydrogels were administered via syringe injection near the tumor site under anesthesia. Mice were assigned to six experimental groups (n = 5 per group) based on the hydrogel formulation used: (1) control group (no treatment), (2) PF-127 hydrogel containing SN-38-chol NPs, (3) APF hydrogel containing SN-38-chol NPs, (4) APF hydrogel with PDA NPs + NIR irradiation, (5) APF hydrogel co-loaded with irinotecan and PDA NPs + NIR irradiation, and (6) APF hydrogel co-loaded with SN-38-chol NPs and PDA NPs + NIR irradiation. Each hydrogel formulation contained a drug concentration of 31.2 nmol. The hydrogels used in the experiment measured approximately 0.8 cm  $\times$  $0.8 \text{ cm} \times 0.2 \text{ cm}$ .

#### 4.8. In vivo NIR-responsiveness of hydrogels

Three days after hydrogel implantation, an 808 nm laser was applied to the hydrogel near the wound site at a power density of 4 W cm<sup>-2</sup> for 5 minutes. A thermography camera was used to monitor temperature changes at the irradiated area, capturing data at 30-second intervals. The initial temperature before irradiation was set at 25 °C.

#### 4.9. Antitumor effect of SN-38-chol NPs-loaded hydrogel

The hydrogels were injected near the tumor sites in mice, followed by weekly NIR irradiation (808 nm) for 5 minutes under anesthesia. The power density of the NIR light was set at 4 W cm<sup>-2</sup>, and temperature variations during irradiation were recorded.

Following hydrogel implantation, tumor size and body weight were measured twice per week. On day 21, the mice were euthanized using sevoflurane anesthesia, and the tumors were excised for weight measurement. The hydrogel implantation was designated as day 0, and tumor size measurements were referenced accordingly. Relative tumor size was determined at each measurement point based on the initial tumor size. Tumor volume (V) was calculated using the following formula:

$$V [\text{mm}^3] = (L [\text{mm}] \times W^2 [\text{mm}^2])/2$$

where L represents the longest tumor diameter, and W denotes the largest perpendicular transverse diameter.

#### 4.10. Side effect

Tracking fluctuations in mouse body weight offers key insights into the systemic effects and potential adverse reactions of drug-loaded hydrogel treatment, serving as an indicator of overall health status. On day 21 following hydrogel administration, hematological analysis was performed to evaluate myelosuppression. The procedure began with disinfecting the tail, followed by a small incision ( $\sim 0.5$  cm) using scissors. A capillary tube was used to collect roughly 30 µL of blood, and hemostasis was achieved by applying light pressure to the incision site.

For white blood cell quantification, a 10 µL blood sample was diluted 20-fold with Turk's staining solution (Nacalai, Kyoto, Japan). This reagent selectively lysed erythrocytes and platelets while staining leukocyte nuclei, allowing enumeration under a hemocytometer. For red blood cell analysis, a 10 µL sample was diluted 400-fold using Hayem's solution (Muto Pure Chemicals, Tokyo, Japan). This solution facilitated selective lysis of white blood cells, enabling accurate red blood cell counting.

#### Conflicts of interest

There are no conflicts to declare

## Data availability

All relevant data are within the manuscript and the ESI.† The data supporting this study's findings are available from the corresponding author upon reasonable request.

# Acknowledgements

A part of this study was supported by Research equipment sharing system, Tohoku University (094 Ultra-fast Raman imaging). This work was supported by JSPS Grants-in-Aid for Scientific Research (No. 22H00328, 23K14316), the Cooperative Research Program of 'Network Joint Research Center for Materials and Devices', and the Research Program of 'Dynamic Alliance for Open Innovation Bridging Human, Environment and Materials' in 'Network Joint Research Center for Materials and Devices'.

#### References

- 1 K. B. Tran, J. J. Lang, K. Compton, R. Xu, A. R. Acheson, H. J. Henrikson, J. M. Kocarnik and L. Penberthy, et al., Lancet, 2022, 400, 563-591.
- 2 B. Han, R. Zheng, H. Zeng, S. Wang, K. Sun, R. Chen, L. Li, W. Wei and J. He, J. Natl. Cancer Center, 2024, 4, 47-53.
- 3 U. Anand, A. Dey, A. K. S. Chandel, R. Sanyal, A. Mishra, D. K. Pandey, V. De Falco, A. Upadhyay, R. Kandimalla, A. Chaudhary, J. K. Dhanjal, S. Dewanjee, J. Vallamkondu and J. M. Pérez de la Lastra, Genes Dis., 2022, DOI: 10.1016/ j.gendis.2022.02.007.

- 4 B. Liu, H. Zhou, L. Tan, K. T. H. Siu and X. Y. Guan, Signal Transduction Targeted Ther., 2024, DOI: 10.1038/s41392-024-01856-7.
- 5 Z. N. Lei, Q. Tian, Q. X. Teng, J. N. D. Wurpel, L. Zeng, Y. Pan and Z. S. Chen, MedComm, 2023, DOI: 10.1002/mco2.265.
- 6 Y. P. Chen, N. Ismaila, M. L. Chua, A. D. Colevas, R. Haddad, S. H. Huang, J. T. Wee, A. C. Whitley, J. L. Yi, S. S. Yom and A. T. Chan, J. Clin. Oncol., 2021, 39, 840-859.
- 7 F. Xie, S. Tang, Y. Zhang, Y. Zhao, Y. Lin, Y. Yao, M. Wang, Z. Gu and J. Wan, ACS Nano, 2024, 18, 1690-1701.
- 8 F. Jin, J. Qi, D. Liu, Y. You, G. Shu, Y. Du, J. Wang, X. Xu, X. Ying, J. Ji and Y. Du, J. Controlled Release, 2021, 337, 90-104.
- 9 Y. Di, H. Zhang, Z. Luo, C. Feng, X. Zhang, S. Yang, J. Hou and L. Yan, Polym. Chem., 2024, 15, 2883-2898.
- 10 S. S. Zargarian, B. Kupikowska-Stobba, A. Kosik-Kozioł, M. Bartolewska, A. Zakrzewska, D. Rybak, K. Bochenek, M. Osial and F. Pierini, Mater. Today Chem., 2024, 41, DOI: 10.1016/j.mtchem.2024.102281.
- 11 M. Bashiru, S. Macchi, M. Forson, A. Khan, A. Ishtiaq, A. Oyebade, A. Jalihal, N. Ali, R. J. Griffin, A. K. Oyelere, N. Hooshmand and N. Siraj, ACS Appl Nano Mater, 2024, 7, 2176-2189.
- 12 Z. Wang, S. Pang, X. Liu, Z. Dong, Y. Tian, M. Ashrafizadeh, N. Rabiee, Y. N. Ertas and Y. Mao, Int. J. Biol. Macromol., 2024, DOI: 10.1016/j.ijbiomac.2024.132579.
- 13 W. Islam, T. Niidome and T. Sawa, J. Pers. Med., 2022, DOI: 10.3390/jpm12121964.
- 14 K. Elumalai, S. Srinivasan and A. Shanmugam, Biomed. Technol., 2024, DOI: 10.1016/j.bmt.2023.09.001.
- 15 C. P. Hollis, H. L. Weiss, M. Leggas, B. M. Evers, R. A. Gemeinhart and T. Li, J. Controlled Release, 2013, 172, 12-21.
- 16 S. Datta and D. J. W. Grant, Nat. Rev. Drug Discovery, 2004, DOI: 10.1038/nrd1280.
- 17 N. Parveen, M. A. S. Abourehab, P. V. Thanikachalam, R. K. Khar and P. Kesharwani, Colloids Surf., B, 2023, DOI: 10.1016/j.colsurfb. 2023.113231.
- 18 M. Malamatari, K. M. G. Taylor, S. Malamataris, D. Douroumis and K. Kachrimanis, Drug Discovery Today, 2018, DOI: 10.1016/j.drudis.2018.01.016.
- 19 N. Paredes da Rocha, A. de Souza, M. Nishitani Yukuyama, T. Lopes Barreto, L. de, O. Macedo, R. Löbenberg, G. Lima Barros de Araújo, K. Ishida and N. Araci Bou-Chacra, *Int.* J. Pharm., 2023, DOI: 10.1016/j.ijpharm.2022.122428.
- 20 H. Kasai, T. Murakami, Y. Ikuta, Y. Koseki, K. Baba, H. Oikawa, H. Nakanishi, M. Okada, M. Shoji, M. Ueda, H. Imahori and M. Hashida, Angew. Chem., Int. Ed., 2012, 51, 10315-10318.
- 21 H. Kasai, H. S. Nalwa, H. Oikawa, S. Okada, H. Matsuda, N. Minami, A. Kakuta, K. Ono, A. Mukoh and H. N. H. Nakanishi, Jpn. J. Appl. Phys., 1992, 31(8A), L1132.
- 22 K. Tanita, Y. Koseki, K. Shimizu, H. Umezawa and H. Kasai, Mol. Cryst. Liq. Cryst., 2020, 706, 79-85.

- 23 Y. Ikuta, Y. Koseki, T. Onodera, H. Oikawa and H. Kasai, Chem. Commun., 2015, 51, 12835-12838.
- 24 Y. Koseki, Y. Ikuta, L. Cong, M. Takano-Kasuya, H. Tada, M. Watanabe, K. Gonda, T. Ishida, N. Ohuchi, K. Tanita, F. Taemaitree, A. T. N. Dao, T. Onodera, H. Oikawa and H. Kasai, Bull. Chem. Soc. Jpn., 2019, 92, 1305-1313.
- 25 A. Shibata, Y. Koseki, K. Tanita, R. Suzuki, A. T. N. Dao and H. Kasai, Tetrahedron Lett., 2022, DOI: 10.1016/j.tetlet. 2022.153989.
- 26 Y. Zhang, X. Zhan, J. Xiong, S. Peng, W. Huang, R. Joshi, Y. Cai, Y. Liu, R. Li, K. Yuan, N. Zhou and W. Min, Sci. Rep., 2018, DOI: 10.1038/s41598-018-26978-1.
- 27 G. Ou, Z. Li, D. Li, L. Cheng, Z. Liu and H. Wu, Nano Res., 2016, 9, 1236-1243.
- 28 J. Lu, L. Cai, Y. Dai, Y. Liu, F. Zuo, C. Ni, M. Shi and J. Li, The Chemical Record, 2021, DOI: 10.1002/tcr.202000170.
- 29 W. Zhong, K. H. Wong, F. Xu, N. Zhao and M. Chen, Acta Biomater., 2022, 145, 135-145.
- 30 J. Zhu, Z. Wang, X. Xu, M. Xu, X. Yang, C. Zhang, J. Liu, F. Zhang, X. Shuai, W. Wang and Z. Cao, Mol. Pharm., 2020, 17, 817-826.
- 31 B. Chehri, K. Liu, G. Vaseghi, A. Seyfoori and M. Akbari, Cells, 2024, DOI: 10.3390/cells13040363.
- 32 L. Wang, Y. Luo, Y. Song, X. He, T. Xu and X. Zhang, ACS Nano, 2024, 18, 3468-3479.
- 33 X. Cao, C. Yang, X. Zhu, M. Zhao, Y. Yan, Z. Huang, J. Cai, J. Zhuang, S. Li, W. Li and B. Shen, Chin. Chem. Lett., 2024, DOI: 10.1016/j.cclet.2023.109199.
- 34 S. S. Zargarian, C. Rinoldi, Y. Ziai, A. Zakrzewska, R. Fiorelli, M. Gazińska, M. Marinelli, M. Majkowska, P. Hottowy, B. Mindur, R. Czajkowski, E. Kublik, P. Nakielski, M. Lanzi, L. Kaczmarek and F. Pierini, Small Sci., 2025, DOI: 10.1002/ smsc.202400463.
- 35 R. Nair, P. Paul, I. Maji, U. Gupta, S. Mahajan, M. Aalhate, S. K. Guru and P. K. Singh, Carbohydr. Polym., 2024, DOI: 10.1016/j.carbpol.2023.121644.
- 36 J. Lee and S. J. Choi, J. Food Eng., 2025, DOI: 10.1016/ j.jfoodeng.2025.112540.
- 37 M. R. Pouso, B. L. Melo, J. J. Gonçalves, A. G. Mendonça, I. J. Correia and D. de Melo-Diogo, Eur. J. Pharm. Biopharm., 2024, DOI: 10.1016/j.ejpb.2024.114476.
- 38 R. J. PJ, O. S. Oluwafemi, S. Thomas and A. O. Oyedeji, J. Drug Delivery Sci. Technol., 2022, DOI: 10.1016/ j.jddst.2022.103390.
- 39 P. A. N. S. Priyadharshana, J. Y. Park, S. H. Hong and J. K. Song, Small, 2022, DOI: 10.1002/smll.202203551.
- 40 F. E. Antunes, L. Gentile, C. Oliviero Rossi, L. Tavano and G. A. Ranieri, Colloids Surf., B, 2011, 87, 42-48.
- 41 M. Dewan, G. Sarkar, M. Bhowmik, B. Das, A. K. Chattoapadhyay, D. Rana and D. Chattopadhyay, Int. J. Biol. Macromol., 2017, 102, 258-265.
- 42 M. Y. Yeh, J. Y. Zhao, Y. R. Hsieh, J. H. Lin, F. Y. Chen, R. D. Chakravarthy, P. C. Chung, H. C. Lin and S. C. Hung, RSC Adv., 2017, 7, 21252-21257.
- 43 A. Wang, L. Dong, Z. Guo, W. Sun and S. Mi, Biomed. Mater., 2022, DOI: 10.1088/1748-605X/ac6ea9.

- 44 S. H. Chuang, K. J. Chen, Y. T. Cheng, Y. S. Chen, S. Y. Lin, H. Y. Chou and H. C. Tsai, *Int. J. Biol. Macromol.*, 2024, DOI: 10.1016/j.ijbiomac.2024.135894.
- 45 Y. Liu, X. Wei, T. Yang, X. Wang, T. Li, M. Sun, K. Jiao, W. Jia, Y. Yang, Y. Yan, S. Wang, C. Wang, L. Liu, Z. Dai, Z. Jiang, X. Jiang, C. Li, G. Liu, Z. Cheng and Y. Luo, *Int. J. Biol. Macromol.*, 2024, DOI: 10.1016/j.ijbiomac.2024. 136085.
- 46 D. B. Mahmoud, C. Wölk and M. Schulz-Siegmund, *Adv. Healthc. Mater.*, 2023, DOI: 10.1002/adhm.202301643.
- 47 L. Wan, P. Li, M. Yan, J. Wang and X. Li, Eur. Polym. J., 2023, DOI: 10.1016/j.eurpolymj.2023.112034.
- 48 D. Jaque, L. Martínez Maestro, B. Del Rosal, P. Haro-Gonzalez, A. Benayas, J. L. Plaza, E. Martín Rodríguez and J. García Solé, *Nanoscale*, 2014, 6, 9494–9530.
- 49 P. Chang, Y. Guo, D. Chen, K. Li, W. Wang, Z. Yang, J. Ma, Y. Zeng, W. Zhan and Y. Zhan, *J. Nanobiotechnol.*, 2024, DOI: 10.1186/s12951-024-02653-8.
- 50 S. Ma, D. Li, X. Jia, W. Xu, G. Ding, J. He and J. Wang, Adv. Funct. Mater., 2024, DOI: 10.1002/adfm.202402692.
- 51 M. Elmowafy, N. K. Alruwaili, K. Shalaby, K. S. Alharbi, W. M. Altowayan, N. Ahmed, A. Zafar and M. Elkomy, *Pharmaceutics*, 2020, DOI: 10.3390/pharmaceutics12020160.
- 52 M. E. Dmitrenko, A. V. Penkova, R. R. Atta, A. A. Zolotarev, T. V. Plisko, A. S. Mazur, N. D. Solovyev and S. S. Ermakov, *Mater. Des.*, 2019, DOI: 10.1016/j.matdes.2019.107596.

- 53 B. Samiey and F. Ashoori, *Chem. Cent. J.*, 2012, DOI: 10.1186/ 1752-153X-6-14.
- 54 L. Hadidi, E. Davari, M. Iqbal, T. K. Purkait, D. G. Ivey and J. G. C. Veinot, *Nanoscale*, 2015, 7, 20547–20556.
- 55 M. Kciuk, B. Marciniak and R. Kontek, *Int. J. Mol. Sci.*, 2020, DOI: 10.3390/ijms21144919.
- 56 L. Ning, C. You, Y. Zhang, X. Li and F. Wang, Compos. Commun., 2021, DOI: 10.1016/j.coco.2021.100739.
- 57 Y. Lu, Y. Li and W. Wu, *Acta Pharm. Sin. B*, 2016, **6**(2), 106–113, DOI: **10.1016/j.apsb.2015.11.005**.
- 58 Z. Liu, Y. Koseki, R. Suzuki, A. T. N. Dao and H. Kasai, *Macromol. Biosci.*, 2025, DOI: 10.1002/mabi.202400413.
- 59 K. Sharun, S. A. Banu, M. Mamachan, R. S. Emmanuel, R. Kumar, O. R. Vinodhkumar, K. Dhama, A. M. Pawde, S. K. Maiti and A. Pal, *Discovery Med.*, 2024, 36, 294.
- 60 Y. Y. Chen, H. C. Wu, J. S. Sun, G. C. Dong and T. W. Wang, Langmuir, 2013, 29, 3721–3729.
- 61 M. P. Bomediano, L. C. E. da Silva, P. Mota-Santiago, M. G. de Oliveira and T. S. Plivelic, Front. Soft Matter., 2024, DOI: 10.3389/frsfm.2024.1354122.
- 62 D. Rybak, J. Du, P. Nakielski, C. Rinoldi, A. Kosik-Kozioł, A. Zakrzewska, H. Wu, J. Li, X. Li, Y. Yu, B. Ding and F. Pierini, Adv. Healthc. Mater., 2025, DOI: 10.1002/adhm.202404274.
- 63 M. Yang, A. T. Dao, H. Nakatani, Y. Eguchi, R. Suzuki, Y. Koseki, K. Oka and H. Kasai, MRS Commun., 2025, 1–8.